Published in final edited form as:
Mol Cell. 2023 November 02; 83(21): 3931–3939.e5. doi:10.1016/j.molcel.2023.09.025.

Identification of Hyperoxidized PRDX3 as a Ferroptosis Marker Reveals Ferroptotic Damage in Chronic Liver Diseases

Shaojie Cui[1,*], **Anchal Ghai**[2], **Yaqin Deng**[1], **Shili Li**[1], **Ruihui Zhang**[3], **Christopher Egbulefu**[2], **Guosheng Liang**[1,4], **Samuel Achilefu**[2], **Jin Ye**[1,5,*]

[1]Department of Molecular Genetics, University of Texas Southwestern Medical Center, Dallas, Texas, USA.

[2]Department of Biomedical Engineering, University of Texas Southwestern Medical Center, Dallas, Texas, USA.

[3]Department of Molecular Biology, University of Texas Southwestern Medical Center, Dallas, Texas, USA.

[4]Center for Human Nutrition, University of Texas Southwestern Medical Center, Dallas, Texas, USA.

[5]Lead contact

Abstract

Ferroptosis, a regulated cell death pathway driven by accumulation of phospholipid peroxides, has been challenging to identify in physiological conditions owing to the lack of a specific marker. Here we identify hyperoxidized peroxiredoxin 3 (PRDX3) as a marker for ferroptosis both *in vitro* and *in vivo*. During ferroptosis, mitochondrial lipid peroxides trigger PRDX3 hyperoxidation, a posttranslational modification that converts a Cys thiol to sulfinic or sulfonic acid. Once hyperoxidized, PRDX3 translocates from mitochondria to plasma membranes where it inhibits cystine uptake, thereby causing ferroptosis. Applying hyperoxidized PRDX3 as a marker, we determined that ferroptosis is responsible for death of hepatocytes in mouse models of both alcoholic and nonalcoholic fatty liver diseases, the most prevalent chronic liver disorders. Our

---

[*] Correspondence: Shaojie.cui@utsouthwestern.edu; jin.ye@utsouthwestern.edu.

Author contributions:
Conceptualization: SC, SA, GL, JY
Methodology: SC, SA, GL, JY
Investigation: SC, AG, YD, SL, RZ, CE
Visualization: SC
Funding acquisition: JY
Project administration: JY, SA, GL
Supervision: JY, SA, GL
Writing – original draft: SC, SL, GL, JY
Writing – review & editing: SC, AG, YD, SL, CE, SA, GL, JY

DECLARATION OF INTERESTS
The authors declare no competing interests.

study highlights the importance of ferroptosis in pathophysiological conditions, and opens the possibility to treat these liver diseases with drugs that inhibit ferroptosis.

Graphical Abstract

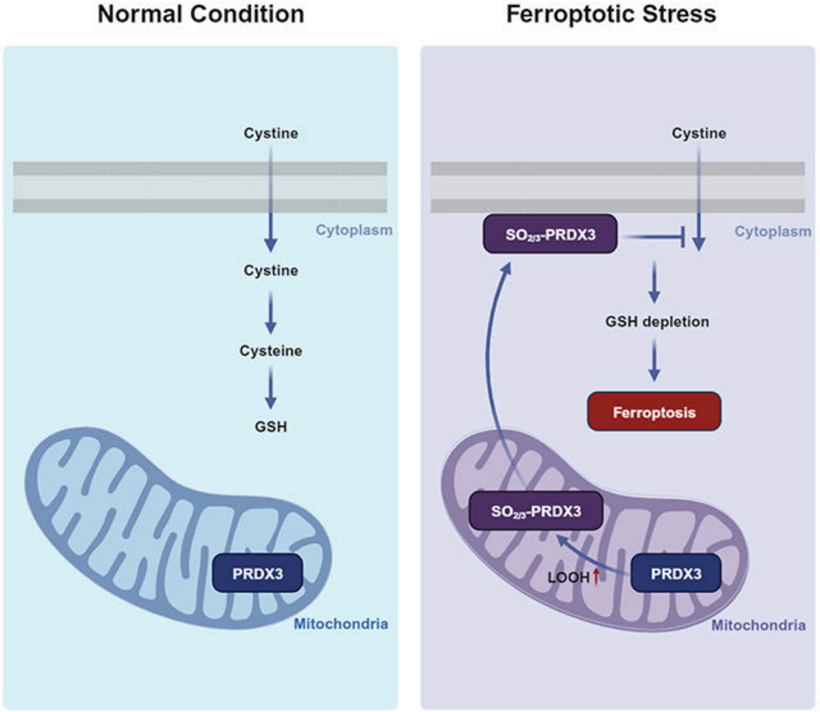

eTOC Blurb

Cui et al. identify hyperoxidized PRDX3 as a marker for ferroptosis both *in vitro* and *in vivo*. Applying this marker, they demonstrate that hepatic damage in mouse models of AFLD and NAFLD, the most prevalent chronic liver diseases in humans, is caused by ferroptosis.

Keywords

ferroptosis; cell death marker; PRDX3; hyperoxidation; AFLD and NAFLD

Introduction

Ferroptosis is a regulated cell death pathway triggered by iron-catalyzed accumulation of phospholipid peroxides[1]. Glutathione peroxidase 4 (GPX4), which reduces phospholipid peroxides using glutathione (GSH) as the reductant, is critical to protect mammalian cells from ferroptosis. Thus, compounds inhibiting GPX4 have been developed as essential tools to stimulate ferroptosis[1,2]. These compounds include RSL3 that directly inhibit GPX4 activity through covalent modification[3], FIN56 that stimulates GPX4 degradation[4], and erastin and its derivative erastin2 that indirectly inhibit GPX4 by depleting GSH through inhibiting system x_c^--mediated cystine uptake[5,6]. While these compounds enable studies of ferroptosis *in vitro*, identification of ferroptotic cells under physiological contexts remains challenging owing to the lack of a marker specific to ferroptosis[1]. To solve this problem, a tremendous progress has been made by demonstrating that increased cell surface localization of transferrin receptor 1 (TfR1) was associated with ferroptosis[7]. However, TfR1 is present on the cell surface even under normal circumstances, and cell surface localization of TfR1 can also be regulated by other factors such as the availability of its ligand[8]. Thus, a more sensitive and specific marker is needed to detect ferroptotic cells[1].

In the current study, we identified hyperoxidized peroxiredoxin 3 (PRDX3) as a marker for ferroptosis both *in vitro* and *in vivo*. Applying this marker, we determined that it is ferroptosis that contributes to hepatic damage in mouse models of alcoholic and nonalcoholic fatty liver diseases (AFLD and NAFLD).

Results and Discussion

PRDX3 is hyperoxidized in ferroptotic cells

The identification of cleaved caspase 3 and phosphorylated mixed lineage kinase domain-like protein (p-MLKL) as markers for apoptosis and necroptosis, respectively[9,10], is essential to detect cells undergoing these cell death pathways. These markers are activated through posttranslational modifications that rapidly transmit death signals to execute cell demise. To identify markers for ferroptosis, we searched for proteins that can be posttranslationally modified by peroxides that accumulate in ferroptotic cells. PRDXs have been known to subject to hyperoxidation, a self-catalyzed posttranslational modification using peroxides as substrates[11]. Under normal circumstances, typical 2-Cys PRDXs, which include PRDX1, PRDX2, PRDX3 and PRDX4, use a catalytic Cys to reduce peroxides. The Cys sulfenic acid (Cys-SOH) produced by the reaction leads to formation of a disulfide-linked homodimer, and the reduction of which allows the enzymes to continue their catalytic cycle (Figure 1A, reactions 1-3). Upon accumulation of excess peroxides, the rate of disulfide bond formation is not fast enough to prevent the Cys-SOH in PRDXs from further oxidation by the peroxides to generate Cys sulfinic (Cys-SO_2H) and sulfonic acid (Cys-SO_3H), the hyperoxidation products of PRDXs (Figure 1A, reactions 4 and 5). Thus, the accumulation of lipid peroxides in ferroptotic cells may be sensed by PRDXs, resulting in hyperoxidation of the proteins. To test this hypothesis, we performed immunoblot analysis with an antibody recognizing a peptide containing Cys-$SO_{2/3}H$ of PRDX1-4, the sequence of which is indistinguishable among all four PRDXs. While barely any signal was detected in untreated transformed human fibroblasts SV589 cells, a single band of ~23 kDa was observed in cells treated with compounds that cause ferroptosis such as erastin (Figure 1B), RSL3 (Figure 1C), or FIN56 (Figure 1D) in a concentration-dependent manner. The detection of this ~23 kDa band was blocked by co-incubation of the antibody with the hyperoxidized antigenic but not by unmodified control peptide during the immunoblot analysis, indicating that this antibody specifically targets hyperoxidized PRDX1-4 (Figure S1A). In contrast to the hyperoxidized form of PRDXs, none of these treatments altered the total amount of PRDX1-4 (Figures 1B-1D). We previously reported that upon cotreatment with arachidonate (AA), a low dose of RSL3 was sufficient to trigger ferroptosis in cells deficient in Fas-associated factor 1 (FAF1) but not wild-type (WT) cells[12]. Consistently, treatment with AA plus RSL3 resulted in the appearance of the ~23 kDa band detected by anti-hyperoxidized PRDX1-4 in *FAF1*$^{-/-}$ but not WT cells (Figure S1B).

Since PRDX1-4 have different molecular weight (Figure S1C), the observation that the anti-hyperoxidized PRDX1-4 only detected a single band of ~23 kDa in ferroptotic cells suggests that only one PRDX was hyperoxidized under this condition. Comparison of the molecular weight on SDS-PAGE indicated that the hyperoxidized PRDX induced by erastin or its more potent derivative erastin2[6] comigrated with PRDX3 (Figure 1E) but not other PRDXs (Figure S1C and S1D). Thus, ferroptosis appeared to specifically induce hyperoxidation of PRDX3. This conclusion was further supported by observations that the hyperoxidized PRDX generated in erastin-treated cells can be immunoprecipitated with anti-PRDX3 (Figure 1F) and was no longer detectable in *PRDX3*$^{-/-}$ cells (Figure 1G). Among PRDX1-4, PRDX3 is the peroxidase located in mitochondria[13], in which lipid peroxides are known to accumulate during ferroptosis[14,15]. Thus, PRDX3 hyperoxidation may be a mechanism to sense excess mitochondrial lipid peroxides produced in ferroptotic cells. In addition to SV589 cells used in experiments shown above, erastin and RSL3 also triggered hyperoxidation of PRDX3 in human fibrosarcoma HT1080 cells, lung carcinoma A549 cells, hepatoma Huh7 cells, and colorectal adenocarcinoma HT29 cells in a concentration-dependent manner (Figures 1H-1K).

Besides the typical 2-Cys PRDXs (PRDX1-4), mammalian cells also express an atypical 2-Cys PRDX, PRDX5, and a 1-Cys PRDX, PRDX6[16]. Only PRDX6 but not PRDX5 was observed to undergo hyperoxidation in cultured cells[17]. In contrast to PRDX3, hyperoxidation of PRDX6 was inhibited in ferroptotic cells treated with erastin (Figure S1E). Thus, among all the PRDXs, PRDX3 is specifically hyperoxidized during ferroptosis.

Hyperoxidized PRDX3 stimulates ferroptosis by inhibiting cystine uptake

To determine whether hyperoxidized PRDX3 marks for ferroptosis, a clear understanding of its role in the cell death pathway is essential. Time course experiments revealed that it took erastin 9 hours to abruptly induce hyperoxidation of PRDX3 in an all-or-none fashion (Figure 2A). This pattern of induction made the time-course experiments an ideal approach to determine the roles of hyperoxidized PRDX3 in ferroptosis, as the effect of the protein can be studied by adjusting the erastin treatment time. Before the 9-hour time point at which hyperoxidized PRDX3 was produced in WT cells, both WT and *PRDX3*$^{-/-}$ cells proliferated at a similar rate (Figure 2A). These results suggest that the lack of the unmodified PRDX3 did not affect viability of the cells treated with erastin. After the 9-hour point, WT cells started to perish whereas *PRDX3*$^{-/-}$ cells continued to proliferate (Figure 2A). These observations suggest that the resistance of *PRDX3*$^{-/-}$ cells to erastin-triggered ferroptosis may be owing to the lack of hyperoxidized PRDX3. Consistent with this observation, a dose curve analysis revealed that knockout of *PRDX3* caused marked resistance of cells to erastin-induced ferroptosis (Figure 2B). This difference in cell viability was eliminated once *PRDX3* expression was restored in *PRDX3*$^{-/-}$ cells (Figures S2A and S2B). To rule out the possibility that compensatory overexpression of other PRDXs in *PRDX3*$^{-/-}$ cells may cause their resistance to ferroptosis, we measured levels of all PRDXs in these cells. This analysis revealed that the expression level of PRDX5 but not other PRDXs was elevated in *PRDX3*$^{-/-}$ cells (Figure S2C). However, overexpression of PRDX5 in WT cells did not result in marked resistance to ferroptosis shown in *PRDX3*$^{-/-}$ cells (Figures S2D and S2E). These results suggest that the resistance of *PRDX3*$^{-/-}$ cells to ferroptosis was primarily caused by PRDX3 depletion. Notably, this effect was not unique to SV589 cells, as knockout *PRDX3* also rendered HT1080 cells more resistant to erastin-induced ferroptosis (Figure S2F). We then assessed the impact of hyperoxidized PRDX3 on ferroptosis induced by other compounds. Results similar to that of erastin were obtained from SAS, which also induces ferroptosis by inhibiting cystine uptake[6] (Figure S2G). In contrast, cells deficient in PRDX3 only exhibited slight resistance to RSL3 and FIN56, which stimulate ferroptosis through a different mechanism that does not affect cystine uptake (Figures 2C and 2D).

The results shown above suggest that hyperoxidized PRDX3 is more involved in erastin and SAS-induced ferroptosis. In contrast to RSL3 and FIN56, erastin and SAS indirectly inhibits GPX4 by GSH depletion[3]. Accordingly, we observed that erastin treatment reduced the total amount of GSH in WT but not *PRDX3*$^{-/-}$ cells (Figure 2E). Consequently, expression of SLC7A11, which encodes the light chain of system x_c^- that is induced in response to GSH depletion[5], was enhanced in WT but not *PRDX3*$^{-/-}$ cells treated with erastin (Figure S2H). These observations suggest that in the absence of hyperoxidized PRDX3, the availability of GSH enabled GPX4 to effectively remove lipid peroxides in erastin-treated *PRDX3*$^{-/-}$ cells, rendering them resistant to ferroptosis. To test this hypothesis, we measured the amount of lipid peroxides using BODIPY 581/591 C11, a fluorescent probe that shifts its emission from red to green upon oxidation by lipid peroxides[18]. Both flow cytometry and immunofluorescent microscopy analysis indicated that BODIPY 581/591 C11 was oxidized in WT but not *PRDX3*$^{-/-}$ cells treated with erastin or erastin2 (Figures 2F and S2I), observations supporting our hypothesis.

Immunofluorescent microscopy analysis indicated that in contrast to PRDX3 that resided in mitochondria, the hyperoxidized PRDX3 was located on plasma membranes (Figures 2G and S2J). Considering that cystine uptake, a reaction also occurring at plasma membranes, is critical to maintain intracellular levels of GSH, we examined the effect of hyperoxidized PRDX3 on cystine uptake. As previously reported[3], treatment with erastin resulted in immediate inhibition of cystine uptake (Figure 2H). Under this condition, there was no difference in inhibition of cystine uptake between WT and *PRDX3*$^{-/-}$ cells (Figure 2H), as the erastin treatment was not long enough to produce hyperoxidized PRDX3 in WT cells (Figure 2A). To determine the effect of hyperoxidized PRDX3, we preincubated the cells with erastin for 9 hours, a treatment allowing the production of hyperoxidized PRDX3 in WT cells (Figure 2A), before performing the cystine uptake assay. Under this condition, cystine uptake was inhibited in WT but not *PRDX3*$^{-/-}$ cells (Figure 2H). To determine if the observed difference in cystine uptake was mediated by system x_c^-, the direct target of erastin, we measured glutamate export, as system x_c^- imports cystine in exchange for glutamate in a 1:1 ratio[19]. In contrast to cystine uptake, erastin pretreatment did not prevent the compound from inhibiting glutamate export in either WT or *PRDX3*$^{-/-}$ cells (Figure 2I). Thus, the restoration of cystine uptake in *PRDX3*$^{-/-}$ cells subject to erastin pretreatment was unlikely caused by reactivation of system x_c^-, a notion consistent with reports that erastin directly binds to and irreversibly inhibits the transporter[20,21]. These results suggest that in response to cystine depletion, an alternative cystine transporter distinct from system

x_c^- might be activated; However, this transporter may also be inhibited indirectly by erastin through the production of hyperoxidized PRDX3. This notion is also consistent with previous observations that RSL3 did not reduce the amount of GSH[5], as RSL3-induced generation of hyperoxidized PRDX3 does not inhibit system x_c^--mediated cystine import.

To further confirm that hyperoxidized PRDX3 facilitates ferroptosis by inhibiting cystine uptake, we compared viability of *PRDX3*$^{-/-}$ and that of WT cells in cystine-depleted medium, which does not provide an extracellular source for cystine uptake. Even though hyperoxidized PRDX3 was produced in WT cells upon cystine starvation (Figure S2K), *PRDX3*$^{-/-}$ and WT cells under this condition were equally sensitive to ferroptosis that can be rescued by the ferroptosis inhibitors deferoxamine or ferrostatin-1 (Figure 2J). These results demonstrate that hyperoxidized PRDX3 facilitates ferroptosis through inhibition of cystine import. This mechanism might explain why *PRDX3*$^{-/-}$ cells were more resistant to erastin- than RSL3- or FIN56-induced ferroptosis, as only erastin requires inhibition of cystine import to trigger ferroptosis. This mechanism might also explain previous observations that mitochondria where PRDX3 is located was required for erastin but not RSL3-induced ferroptosis[14,15].

Hyperoxidized PRDX3 is specifically present in ferroptotic cells

Since PRDX3 is hyperoxidized during ferroptosis to execute the cell death pathway, we further evaluated whether hyperoxidized PRDX3 can serve as a marker for ferroptosis by examining the specific presence of the protein in ferroptotic cells. To this end, we observed that cotreatment with deferoxamine, ferrostatin-1, vitamin E or oleate, which inhibits ferroptosis through different mechanism[1,22], prevented erastin or RSL3 from inducing hyperoxidation of PRDX3 (Figures 3A and 3B). In contrast to ferroptosis, hyperoxidized PRDX3 was undetectable in cells subject to apoptosis or necroptosis that is marked by cleaved caspase 3[23] or p-MLKL[10], respectively (Figures 3C and 3D). Hyperoxidized PRDX3 was also not present in cells subject to cuproptosis triggered by the oncology drug elesclomol that causes excessive import of copper[24] (Figure 3E). Inasmuch as mitochondrial oxidative stress occurs during both ferroptosis and cuproptosis[14,25], this observation suggests that hyperoxidized PRDX3 marks for ferroptosis but not mitochondrial oxidative stress. Carbonyl cyanide m-chlorophenyl hydrazone (CCCP) impairs mitochondria through dissipation of mitochondrial membrane potential without causing ferroptosis[14]. Treatment with CCCP markedly reduced the fluorescent intensity of MitoTracker as a result of disappearance of mitochondrial membrane potential (Figure S3A) but failed to induce hyperoxidation of PRDX3 (Figure 3F). These observations confirmed that hyperoxidized PRDX3 marks for ferroptosis but not mitochondrial damage. The specific involvement of hyperoxidized PRDX3 in ferroptosis was further demonstrated by the observations that knockout *PRDX3* did not affect sensitivity of the cells to apoptosis or cuproptosis (Figures S3B and S3C). These results establish hyperoxidized PRDX3 as a ferroptotic marker for cells cultured *in vitro*.

We subsequently employed established mouse models to validate hyperoxidized PRDX3 as an *in vivo* marker for ferroptosis. In the first model, radionuclide stimulated therapy (RaST), which employs Cerenkov-emitting radionuclides to activate a reactive oxygen speciesgenerating photosensitizer, was applied to kill multiple myeloma xenograft in mice[26]. This approach was demonstrated to kill cancer cells through ferroptosis *in vitro*[26]. Using the same antibody that detects hyperoxidized PRDX3, we observed positive immunofluorescent signals on cell surface only in tissue slides containing mouse xenograft tumors subject to RaST but not control treatments (Figures 3G and S3D). In another model, we fed mice with a diet enriched in AA. While the control *Faf1*-floxed mice tolerated this diet, those with liver-specific knockout of *Faf1 (L-Faf1*$^{-/-}$) suffered from hepatic damage that was ameliorated by treatment with liprostatin-1 (Lip-1), a ferroptosis inhibitor[12]. Immunoblot analysis revealed that upon feeding with this diet, hyperoxidized PRDX3 was present in livers of *L-Faf1*$^{-/-}$ but not that of control mice, and the protein was undetectable in that of *L-Faf1*$^{-/-}$ mice treated with Lip-1 (Figure 3H). Similar results were observed through immunofluorescent microscopy (Figures 3I and S3E). Thus, hyperoxidized PRDX3 can also be applied as a marker to identify ferroptotic cells *in vivo*.

The presence of hyperoxidized PRDX3 reveals ferroptotic damage in AFLD and NAFLD

The successful identification of ferroptotic cells in livers prompted us to apply hyperoxidized PRDX3 as a marker to investigate the role of ferroptosis in AFLD and NAFLD, as both diseases are associated with lipid peroxidation[27], the hallmark of ferroptosis[1]. AFLD was suspected to be caused by ferroptosis[28], as alcohol consumption generates conditions that favor ferroptosis, such as increased hepatic iron load, increased hepatic production of superoxide anion radical, and decreased levels of vitamin E[29-31]. Utilizing the NIAAA mouse model of AFLD through chronic and binge feeding with ethanol[32], we observed hepatic damage indicated by elevated serum levels of aspartate transaminase (AST) and alanine transaminase (ALT) in both females and males (Figures 4A and 4B). While hyperoxidized PRDX3 was invisible in mice fed with the control diet, the ferroptotic marker was detected in livers of >70% of mice fed with ethanol regardless of gender (Figure 4C). In contrast, neither cleaved caspase 3 nor p-MLKL was detected in livers of these mice (Figure 4C). To investigate the role of ferroptosis in NAFLD, we used a mouse model by prolonged feeding with a high fat diet (HFD)[33]. This feeding led to the death of hepatocytes reflected by higher AST and ALT levels in serum (Figures 4D and 4E). While hyperoxidized PRDX3 was not detected in livers of the mice fed with a chow diet, the ferroptotic marker was observed in livers of ~70% of the mice fed with the HFD (Figure 4F). In contrast, p-MLKL was undetectable regardless of the diet that was fed, and weak signals of cleaved caspase 3 were observed in mice fed with chow or HFD (Figure 4F). These results demonstrate that ferroptosis contributes to hepatic injury in both AFLD and NAFLD. This conclusion was further supported by the observation that in both AFLD and NAFLD mouse models, hepatic levels of hyperoxidized PRDX3, the marker for ferroptosis, were positively correlated with serum levels of AST and ALT, the markers for hepatic damage (Figures 4G and 4H). These findings support the hypothesis that hepatic damage in AFLD and NAFLD is caused by a similar mechanism[34], and open the possibility to treat both diseases with drugs that inhibit ferroptosis.

Both AFLD and NAFLD encompass a spectrum of diseases that can be developed into steatohepatitis accompanied by severe liver inflammation[34]. While our AFLD mouse model leads to alcoholic steotohepatitis[32], the HFD-induced NAFLD mouse model generally does not advance to the stage of non-alcoholic steatohepatitis (NASH)[35]. Thus, even before progression into NASH, ferroptosis already causes liver damage in NAFLD at an early stage. This observation will enable future studies to determine whether early intervention to inhibit ferroptosis will prevent development of NASH.

Limitations of the study

In this study, we selected the mouse models of AFLD and NAFLD that are most relevant to the human diseases to determine the roles of ferroptosis in development of these diseases. Confirmation of these findings through human studies is challenging owing to the difficulty in obtaining human liver samples, particularly that of healthy controls.

STAR METHODS

Lead Contact

Further information and requests for resources and reagents should be directed to and will be fulfilled by the Lead Contact, Jin Ye (jin.ye@utsouthwestern.edu).

Materials Availability

All unique/stable reagents generated in this study are available from the Lead Contact without restriction.

Data and Code Availability

- Original data for figures in the paper are deposited in Mendeley at https://data.mendeley.com/datasets/hcjytkx35h/draft?a=b5d4b611-f316-4c50-9dd3-6cd5cb0cb487.
- This paper does not report original codes.
- Any additional information required to reanalyze the data reported in this paper is available from the lead contact upon request.

EXPERIMENTAL MODEL AND SUBJECT DETAILS

Animal studies—All animal experiments described in this work were approved and conducted under the oversight of the University of Texas (UT) Southwestern Institutional Animal Care and Use Committee. All mice were housed in colony cages in a room with a 12-h light/12-h dark cycle.

The NIAAA mouse model of AFLD was conducted on littermates of male and female C57BL/6 mice aged between 8 to 23 weeks and 13 to 26 weeks, respectively, in accordance with established protocols[32]. Briefly, the mice were fed with a 5% ethanol-containing Lieber-DeCarli diet (Bio-Serv) for 10 days, followed by a single dose of ethanol (5 g/kg body weight) via gavage on day 11. The pair-fed age-matched control groups were given equivalent volumes of a control liquid diet for 10 days, followed by maltose dextrin via gavage on day 11. The HFD-induced NAFLD mouse model was conducted on 8-week-old C57BL/6 male mice. The mice were randomly separated into two groups: One group of mice ($n = 8$) were fed ad libitum with a chow diet (Teklad global diet 2018) while the other (n=23) were fed ad libitum with a HFD (24% (w/w) fat, 41% (w/w) carbohydrate, and 24% (w/w) casein protein, Research Diet D12451). 12 weeks later, the mice were euthanized at the end of the dark cycle. For both mouse models, following euthanization with isoflurane, blood was collected and the activity of ALT and AST in serum was assayed by the University of Texas Southwestern Metabolic Phenotyping Core.

Cell cultures—*PRDX3*$^{-/-}$ SV589 cells (human male transformed fibroblasts) were generated using the CRISPR/Cas9 approach by transfection of cells with pSpCas9(BB)-2A-Puro (PX459) encoding gRNA targeting *PRDX3* followed by selection and single cell cloning in medium containing 1 μg/ml puromycin. *PRDX3*$^{-/-}$; *pPRDX3* SV589 cells were generated by stably transfecting *PRDX3*$^{-/-}$ cells with pCMV-*PRDX3* followed by selection and single cell cloning in medium containing 700 μg/ml G418. *PRDX5*-overexpression SV589 cells were generated by stably transfecting SV589 cells with pCMV-*PRDX5* followed by selection in medium containing 700 μg/ml G418. *PRDX3*$^{-/-}$ HT1080 cells (human male fibrosarcoma) were generated using the CRISPR/Cas9 approach by transfection of cells with pSpCas9(BB)-2A-Puro (PX459) encoding gRNA targeting *PRDX3* followed by selection in medium containing 0.5 μg/ml puromycin. *FAF1*$^{-/-}$ SV589 cells were generated as previously reported[12]. All SV589-based cells were maintained in Dulbecco's modified Eagle's medium with 1 g/l glucose, 100 IU/ml penicillin, 100 μg/ml streptomycin sulfate, and 5% fetal calf serum, in monolayers at 37°C in 5% CO_2. All HT1080-based cells were maintained in Dulbecco's modified Eagle's medium with 1 g/l glucose, 100 IU/ml penicillin, 100 μg/ml streptomycin sulfate, and 10% fetal calf serum, in monolayers at 37°C in 8% CO_2. A549 cells (human male lung carcinoma) were maintained in 1:1 mixture of Ham's F-12 medium and Dulbecco's modified Eagle's medium containing 100 IU/ml penicillin, 100 μg/ml of streptomycin sulfate, and 5% fetal calf serum, in monolayers at 37°C in 8% CO_2. Huh7 cells[36] (human male hepatoma) were maintained in Dulbecco's modified Eagle's medium with 4.5 g/l glucose, 100 IU/ml penicillin, 100 μg/ml streptomycin sulfate, and 5% fetal calf serum, in monolayers at 37°C in 5% CO_2. HT29 cells (human female colorectal adenocarcinoma) were maintained in 1:1 mixture of Ham's F-12 medium and Dulbecco's modified Eagle's medium containing 100 IU/ml penicillin, 100 μg/ml of streptomycin sulfate, and 10% fetal calf serum, in monolayers at 37°C in 5% CO_2.

To guard against potential genomic instability, an aliquot of each cell line was passaged for only 4 weeks before a fresh batch of cells was thawed and propagated for experimental use.

METHOD DETAILS

Cell viability assay—On day 0, cells were seeded at 1,000 cells per well in 96-well plates. On day 1, cells were treated as described in figure legends. Cell viability was assessed by CellTiter-Glo luminescent cell viability assay according to the manufacturer's recommendations.

Total GSH assay—On day 0, cells were seeded at 400,000 cells per 10 cm plate. On day 1, cells were treated as described in figure legends. Total GSH was assessed by GSH/GSSG-Glo assay according to the manufacturer's recommendations.

Glutamate export assay—On day 0, cells were seeded at 100,000 cells per well in 6-well plates. On day 1, cells were treated as described in figure legends. Glutamate in medium was assessed by Glutamate-Glo assay according to the manufacturer's recommendations.

Cystine uptake assay—Measurement of cystine uptake was carried out as previously described[6]. On day 0, cells were seeded at 150,000 cells per 35-mm dish. On day 1, cells were washed twice in pre-warmed buffer A (137 mM choline chloride, 3 mM KCl, 1 mM $CaCl_2$, 1 mM $MgCl_2$, 5 mM D-glucose, 0.7 mM K_2HPO_4, 10 mM HEPES, pH 7.4) followed by incubation in the buffer for 10 minutes. Cystine uptake was performed in 1 ml buffer A containing 2 μM erastin as indicated and 0.08 μCi (200 mCi/mmol) ^{14}C-Cystine for 5 minutes at 37°C. After washing for three times with ice-cold buffer A, cells were lysed in 1 ml 0.1 M NaOH, and the radioactivity was measured by scintillation counting using Tri-Carb 2800TR (PerkinElmer).

Immunoprecipitation—On day 0, cells were seeded at 400,000 cells per 10 cm plate. On day 1, cells were treated as described in figure legends. the pooled cell pellets from 5 dishes were lysed in buffer B (100 mM Tris-HCl, 150 mM NaCl, 0.1% NP-40, proteinase inhibitor cocktail, pH=7.5). PRDX3 was immunoprecipitated with 10 μg mouse anti-PRDX3 and protein A/G beads in 1ml buffer B for 2 h at 4 °C. Aliquots of input and pellet of the reaction were subject to SDS-PAGE followed by immunoblot analysis as described in the figure legend.

Immunoblot analysis—Cells lysed in buffer C (50 mM Tris-HCl, 150 mM NaCl, 1% NP40, 0.1 % SDS, 0.5% sodium deoxycholate, 1 mM EDTA, protease inhibitor cocktail, pH=7.5) were analyzed by SDS-PAGE followed by immunoblot analysis with the indicated antibodies (1:10,000 dilution for rabbit anti-PRDX1, 1:5,000 dilution for rabbit anti-PRDX2, 1:10,000 dilution for rabbit anti-PRDX3, 1:10,000 dilution for rabbit anti-PRDX4, 1:5,000 dilution for rabbit anti-PRDX5, 1:5,000 dilution for rabbit anti-PRDX6, 1:2,000 dilution for mouse anti-PRDX1, 1:5,000 dilution for mouse anti-PRDX3, 1:2,000 dilution for rabbit anti-$SO_{2/3}$-PRDX1-4, 1:2,000 dilution for rabbit anti-$SO_{2/3}$-PRDX6, 1:10,000 dilution for rabbit anti-SLC7A11, 1:5,000 dilution for rabbit anti-cleaved caspase 3, 1:5,000 dilution for rabbit anti-mouse p-MLKL, 1:10,000 dilution for rabbit anti-human p-MLKL, 1:5,000 dilution for anti-FAF1, 1:10,000 dilution for rabbit anti-Calnexin, and 1:5,000 dilution for rabbit anti-ACTIN). For experiments in Figures 1E and S1D, bound antibodies were visualized with fluorescence-conjugated secondary antibodies (1/5000 dilution for both IRDye® 800CW Goat anti-Rabbit IgG and IRDye® 680LT Goat anti-Mouse IgG) captured by the LI-COR Odyssey Imaging System. For the rest of the experiments, bound primary antibodies were visualized by a peroxidase-conjugated secondary antibody using the SuperSignal West Pico PLUS chemiluminescent substrate system (Thermo Fisher Scientific).

Immunofluorescent microscopy analysis—On day 0, cells were seeded at 100,000 cells per 35-mm glass bottom dish (MatTek). On day 1, they were treated as described in figure legends. On day 2, cells were fixed in cold ethanol, and then permeabilized in phosphate buffer saline (PBS) containing 0.1% TritonX-100. After blocking in PBS containing 5% BSA for 1 h, cells were incubated with rabbit anti-$SO_{2/3}$-PRDX1-4 (1:100 dilution) or mouse anti-PRDX3 (1:500 dilution) diluted in PBS containing 2% BSA buffer overnight at 4 °C. Following wash, cells were stained with 4 μg/ml Alexa Fluor 488 goat anti-mouse IgG and 4 μg/ml Alexa Fluor 633 goat anti-rabbit IgG diluted in PBS containing 2% BSA for 1 hr. The cells were then washed and subjected to confocal imaging analysis using Confocal Zeiss LSM880 Airyscan. Image analysis was performed with Image J software.

For mouse bone tissues containing xenograft tumors, paraffin-embedded sections were treated with xylenes, washed with ethanol, water, and PBS. Antigen retrieval was performed using Buffer D (10 mM Sodium Citrate, 0.05% Tween-20, pH 6.0). Sections were then blocked with PBS containing 0.05% Tween-20 and 5% goat serum for 30 min, incubated with rabbit anti-$SO_{2/3}$-PRDX1-4 (1:100 dilution) overnight in PBS containing 0.05% Tween-20 and 5% BSA at 4°C, washed three times with PBS containing 0.05% Tween-20, then incubated with 4 μg/ml Alexa Fluor 633 goat anti-rabbit IgG diluted in PBS containing 0.05% Tween-20 and 5% BSA at room temperature for 1 h. The slides were then washed and subjected to confocal imaging analysis as described above.

Lipid peroxidation probed by BODIPY 581/591 C11—For fluorescent microscopy, on day 0, cells were seeded at 100,000 cells per 35-mm glass bottom dish (MatTek). On day 1, they were treated as described in legend to Figure S2 and co-incubated with 10 μM BODIPY 581/591 C11 and 1 μg/ml Hoechst 33342 for 10 min before fluorescent microscopy analysis with Confocal Zeiss LSM880 Airyscan equipped with 405 nm, 488 nm, and 560 nm lasers. Image analysis was performed with Image J software. For flow cytometry analysis, on day 0, cells were seeded at 400,000 cells per 10 cm plate. On day 1, they were treated as described in legend to Figure 2 and co-incubated with 10 μM BODIPY 581/591 C11 for 10 min before harvesting. Cells suspended in 200 μl PBS containing 0.1% BSA were subjected to flow cytometry analysis with FL1 filter to detect green fluorescent cells with BD FACSCalibur™ Flow Cytometer. Data were analyzed by the Flow Jo V10 software.

Supplementary Material

Refer to Web version on PubMed Central for supplementary material.

Acknowledgments:

We thank Yanqing Xu for preliminary data that address a reviewer's comment, Lisa Beatty and Alyssa Ayala for cell culture, and Lori Nguyen for technical assistance. This research was funded by National Institutes of Health grant R35-140851 (J.Y.), P01HL160487 (G.L.), and by the UTSWNORC grant P30DK127984 (J.Y., G.L.). The graphic abstract was created through BioRender.com with the license permit number RS25UBIHW9.

Inclusion and Diversity

We support inclusive, diverse, and equitable conduct of research.

Reference

1. Jiang X, Stockwell BR, and Conrad M (2021). Ferroptosis: mechanisms, biology and role in disease. Nat Rev Mol Cell Biol 22, 266–282. 10.1038/s41580-020-00324-8. [PubMed: 33495651]
2. Stockwell BR (2022). Ferroptosis turns 10: Emerging mechanisms, physiological functions, and therapeutic applications. Cell 185, 2401–2421. 10.1016/j.cell.2022.06.003. [PubMed: 35803244]
3. Yang Wan S., SriRamaratnam R, Welsch Matthew E., Shimada K, Skouta R, Viswanathan Vasanthi S., Cheah Jaime H., Clemons Paul A., Shamji Alykhan F., Clish Clary B., et al. (2014). Regulation of ferroptotic cancer cell death by GPX4. Cell 156, 317–331. 10.1016/j.cell.2013.12.010. [PubMed: 24439385]
4. Shimada K, Skouta R, Kaplan A, Yang WS, Hayano M, Dixon SJ, Brown LM, Valenzuela CA, Wolpaw AJ, and Stockwell BR (2016). Global survey of cell death mechanisms reveals metabolic regulation of ferroptosis. Nat Chem Biol 12, 497–503. 10.1038/nchembio.2079. [PubMed: 27159577]
5. Dixon Scott J., Lemberg Kathryn M., Lamprecht Michael R., Skouta R, Zaitsev Eleina M., Gleason Caroline E., Patel Darpan N., Bauer Andras J., Cantley Alexandra M., Yang Wan S., et al. (2012). Ferroptosis: An iron-dependent form of nonapoptotic cell death. Cell 149, 1060–1072. 10.1016/j.cell.2012.03.042. [PubMed: 22632970]
6. Dixon SJ, Patel DN, Welsch M, Skouta R, Lee ED, Hayano M, Thomas AG, Gleason CE, Tatonetti NP, Slusher BS, and Stockwell BR (2014). Pharmacological inhibition of cystine-glutamate exchange induces endoplasmic reticulum stress and ferroptosis. eLife 3, e02523. 10.7554/eLife.02523. [PubMed: 24844246]
7. Feng H, Schorpp K, Jin J, Yozwiak CE, Hoffstrom BG, Decker AM, Rajbhandari P, Stokes ME, Bender HG, Csuka JM, et al. (2020). Transferrin receptor Is a specific ferroptosis marker. Cell Reports 30, 3411–3423.e3417. 10.1016/j.celrep.2020.02.049. [PubMed: 32160546]
8. Gammella E, Buratti P, Cairo G, and Recalcati S (2017). The transferrin receptor: the cellular iron gate. Metallomics 9, 1367–1375. 10.1039/c7mt00143f. [PubMed: 28671201]
9. Galluzzi L, Vitale I, Aaronson SA, Abrams JM, Adam D, Agostinis P, Alnemri ES, Altucci L, Amelio I, Andrews DW, et al. (2018). Molecular mechanisms of cell death: recommendations of the Nomenclature Committee on Cell Death 2018. Cell Death Differ 25, 486–541. 10.1038/s41418-017-0012-4. [PubMed: 29362479]
10. Wang H, Sun L, Su L, Rizo J, Liu L, Wang L-F, Wang F-S, and Wang X (2014). Mixed lineage kinase domain-like protein MLKL causes necrotic membrane disruption upon phosphorylation by RIP3. Mol Cell 54, 133–146. 10.1016/j.molcel.2014.03.003. [PubMed: 24703947]
11. Veal EA, Underwood ZE, Tomalin LE, Morgan BA, and Pillay CS (2017). Hyperoxidation of peroxiredoxins: Gain or loss of function? Antioxid Redox Signal 28, 574–590. 10.1089/ars.2017.7214. [PubMed: 28762774]
12. Cui S, Simmons G, Vale G, Deng Y, Kim J, Kim H, Zhang R, McDonald JG, and Ye J (2022). FAF1 blocks ferroptosis by inhibiting peroxidation of polyunsaturated fatty acids. Proc Natl Acad Sci USA 119, e2107189119. doi:10.1073/pnas.2107189119. [PubMed: 35467977]
13. Araki M, Nanri H, Ejima K, Murasato Y, Fujiwara T, Nakashima Y, and Ikeda M (1999). Antioxidant function of the mitochondrial protein SP-22 in the cardiovascular system. J Biol Chem 274, 2271–2278. 10.1074/jbc.274.4.2271. [PubMed: 9890990]
14. Gao M, Yi J, Zhu J, Minikes AM, Monian P, Thompson CB, and Jiang X (2019). Role of mitochondria in ferroptosis. Mol Cell 73, 354–363.e353. 10.1016/j.molcel.2018.10.042. [PubMed: 30581146]
15. Oh S-J, Ikeda M, Ide T, Hur KY, and Lee M-S (2022). Mitochondrial event as an ultimate step in ferroptosis. Cell Death Discov 8, 414. 10.1038/s41420-022-01199-8. [PubMed: 36209144]
16. Rhee SG, Kang SW, Chang T-S, Jeong W, and Kim K (2001). Peroxiredoxin, a novel family of peroxidases. IUBMB Life 52, 35–41. 10.1080/15216540252774748. [PubMed: 11795591]
17. Woo HA, and Rhee SG (2010). Immunoblot detection of proteins that contain cysteine sulfinic or sulfonic acids with antibodies specific for the hyperoxidized cysteine-containing sequence. In Methods Redox Signal, (Mary Ann Liebert), pp. 19–23.

18. Drummen GPC, van Liebergen LCM, Op den Kamp JAF, and Post JA (2002). C11-BODIPY581/591, an oxidation-sensitive fluorescent lipid peroxidation probe: (micro)spectroscopic characterization and validation of methodology. Free Rad Biol Med 33, 473–490. 10.1016/S0891-5849(02)00848-1. [PubMed: 12160930]
19. Dall'Asta V, Gazzola GC, Franchi-Gazzola R, Bussolati O, Longo N, and Guidotti GG (1983). Pathways of L-glutamic acid transport in cultured human fibroblasts. J Biol Chem 258, 6371–6379. 10.1016/S0021-9258(18)32419-0. [PubMed: 6133863]
20. Yan R, Xie E, Li Y, Li J, Zhang Y, Chi X, Hu X, Xu L, Hou T, Stockwell BR, et al. (2022). The structure of erastin-bound xCT–4F2hc complex reveals molecular mechanisms underlying erastin-induced ferroptosis. Cell Res 32, 687–690. 10.1038/s41422-022-00642-w. [PubMed: 35352032]
21. Sato M, Kusumi R, Hamashima S, Kobayashi S, Sasaki S, Komiyama Y, Izumikawa T, Conrad M, Bannai S, and Sato H (2018). The ferroptosis inducer erastin irreversibly inhibits system x(c)- and synergizes with cisplatin to increase cisplatin's cytotoxicity in cancer cells. Sci Rep 8, 968. 10.1038/s41598-018-19213-4. [PubMed: 29343855]
22. Magtanong L, Ko P-J, To M, Cao JY, Forcina GC, Tarangelo A, Ward CC, Cho K, Patti GJ, Nomura DK, et al. (2019). Exogenous monounsaturated fatty acids promote a ferroptosis-resistant cell state. Cell Chem Biol 26, 420–432.e429. 10.1016/j.chembiol.2018.11.016. [PubMed: 30686757]
23. Porter AG, and Jänicke RU (1999). Emerging roles of caspase-3 in apoptosis. Cell Death Differ 6, 99–104. 10.1038/sj.cdd.4400476. [PubMed: 10200555]
24. Tsvetkov P, Coy S, Petrova B, Dreishpoon M, Verma A, Abdusamad M, Rossen J, Joesch-Cohen L, Humeidi R, Spangler RD, et al. (2022). Copper induces cell death by targeting lipoylated TCA cycle proteins. Science 375, 1254–1261. doi:10.1126/science.abf0529. [PubMed: 35298263]
25. Nagai M, Vo NH, Shin Ogawa L, Chimmanamada D, Inoue T, Chu J, Beaudette-Zlatanova BC, Lu R, Blackman RK, Barsoum J, et al. (2012). The oncology drug elesclomol selectively transports copper to the mitochondria to induce oxidative stress in cancer cells. Free Rad Biol Med 52, 2142–2150. 10.1016/j.freeradbiomed.2012.03.017. [PubMed: 22542443]
26. Zheleznyak A, Mixdorf M, Marsala L, Prior J, Yang X, Cui G, Xu B, Fletcher S, Fontana F, Lanza G, and Achilefu S (2021). Orthogonal targeting of osteoclasts and myeloma cells for radionuclide stimulated dynamic therapy induces multidimensional cell death pathways. Theranostics 11, 7735–7754. 10.7150/thno.60757. [PubMed: 34335961]
27. Bhardwaj P, Madan K, Thareja S, Joshi YK, and Saraya A (2008). Comparative redox status in alcoholic liver disease and nonalcoholic fatty liver disease. Hepatol int 2, 202–208. 10.1007/s12072-008-9060-7. [PubMed: 19669305]
28. You Y, Liu C, Liu T, Tian M, Wu N, Yu Z, Zhao F, Qi J, and Zhu Q (2022). FNDC3B protects steatosis and ferroptosis via the AMPK pathway in alcoholic fatty liver disease. Free Rad Biol Med 193, 808–819. 10.1016/j.freeradbiomed.2022.10.322. [PubMed: 36336231]
29. Li L-X, Guo F-F, Liu H, and Zeng T (2022). Iron overload in alcoholic liver disease: underlying mechanisms, detrimental effects, and potential therapeutic targets. Cell Mol Life Sci 79, 201. 10.1007/s00018-022-04239-9. [PubMed: 35325321]
30. Lu Y, and Cederbaum AI (2008). CYP2E1 and oxidative liver injury by alcohol. Free Radic Biol Med 44, 723–738. 10.1016/j.freeradbiomed.2007.11.004. [PubMed: 18078827]
31. Sandoval C, Farías J, Zamorano M, and Herrera C (2022). Vitamin supplements as a nutritional strategy against chronic alcohol consumption? An updated review. Antioxidants 11, 564. [PubMed: 35326214]
32. Bertola A, Mathews S, Ki SH, Wang H, and Gao B (2013). Mouse model of chronic and binge ethanol feeding (the NIAAA model). Nat Protoc 8, 627. 10.1038/nprot.2013.032. [PubMed: 23449255]
33. Moon Y-A, Liang G, Xie X, Frank-Kamenetsky M, Fitzgerald K, Koteliansky V, Brown Michael S., Goldstein Joseph L., and Horton Jay D. (2012). The Scap/SREBP pathway is essential for developing diabetic fatty liver and carbohydrate-induced hypertriglyceridemia in animals. Cell Metab 15, 240–246. 10.1016/j.cmet.2011.12.017. [PubMed: 22326225]

34. Greuter T, Malhi H, Gores GJ, and Shah VH (2017). Therapeutic opportunities for alcoholic steatohepatitis and nonalcoholic steatohepatitis: exploiting similarities and differences in pathogenesis. JCI Insight 2. 10.1172/jci.insight.95354.
35. Van Herck MA, Vonghia L, and Francque SM (2017). Animal models of nonalcoholic fatty liver disease-A starter's guide. Nutrients 9. 10.3390/nu9101072.
36. Nakabayashi H, Taketa K, Miyano K, Yamane T, and Sato J (1982). Growth of human hepatoma cell lines with differentiated functions in chemically defined medium. Cancer Res. 42, 3858–3863. [PubMed: 6286115]

Highlights:

- PRDX3 is hyperoxidized during ferroptosis but not other cell death pathways.
- Hyperoxidized PRDX3 translocates from mitochondria to plasma membranes.
- Hyperoxidized PRDX3 facilitates ferroptosis by inhibiting cystine uptake.
- Hyperoxidized PRDX3 reveals the contribution of ferroptosis to AFLD and NAFLD.

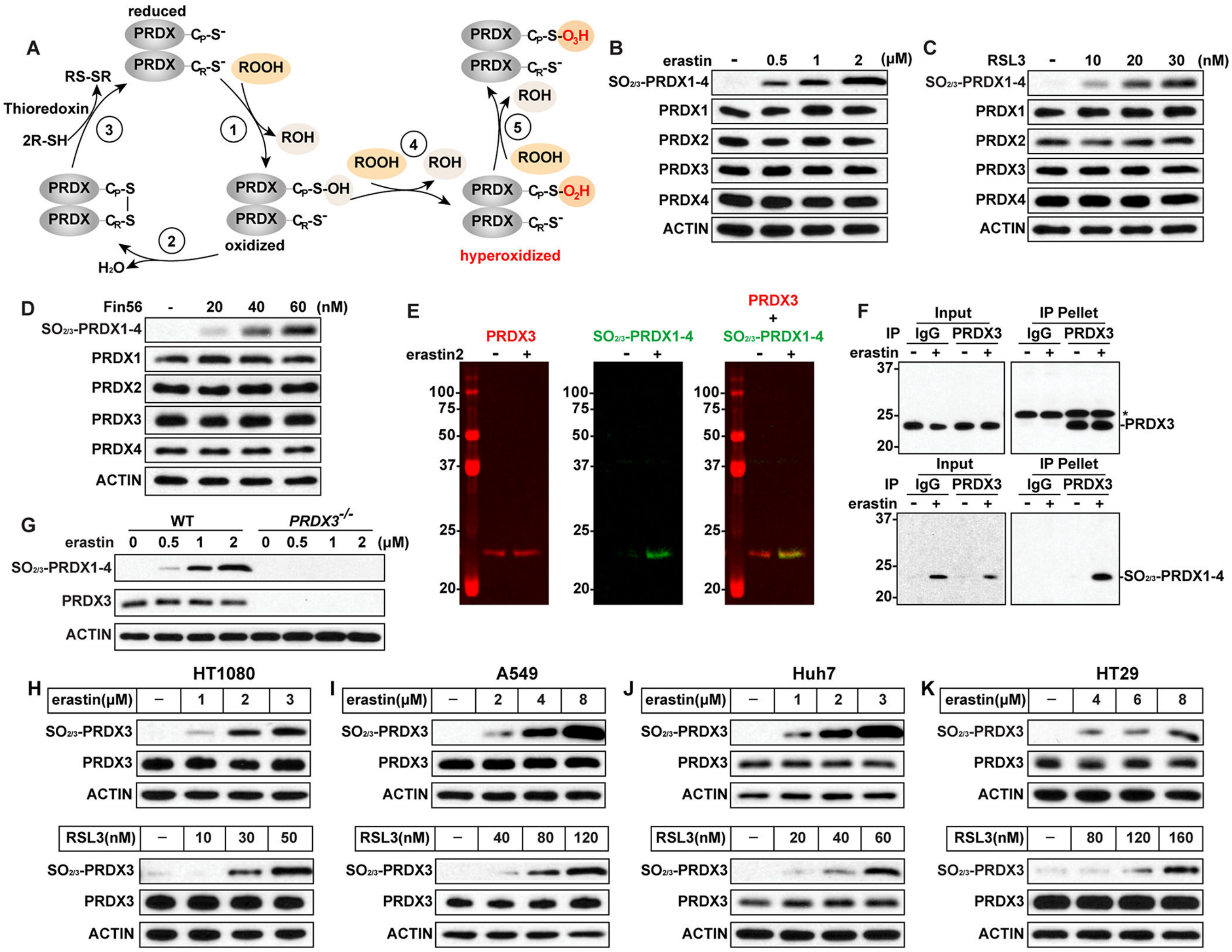

Figure 1. PRDX3 is hyperoxidized during ferroptosis.

(A) Catalytic cycle of PRDXs.

(B-D) Amounts of hyperoxidized and total PRDX1-4 in SV589 cells treated with indicated concentrations of erastin (B), RSL3 (C) or FIN56 (D) for 12 h were determined by immunoblot analysis.

(E) Lysate of cells treated with or without 200 nM erastin2 for 12 h was immunoblotted by anti-PRDX3 and anti-$SO_{2/3}$-PRDX1-4 in the same blot followed by detection with red and green fluorescence-conjugated secondary antibodies, respectively.

(F) Lysate of cells treated with or without 2 μM erastin for 12 h was immunoprecipitated with anti-PRDX3 or control IgG. The input and pellet fractions were analyzed by immunoblot analysis with the indicated antibodies. Asterisk denotes the light chain of the antibodies.

(G) Immunoblot analysis of the indicated cells treated with indicated concentration of erastin for 12 h with anti-$SO_{2/3}$-PRDX1-4 or anti-PRDX3.

(H-K) The amount of hyperoxidized PRDX3 in HT1080 (H), A549 (I), Huh7 (J), and HT29 cells (K) treated with erastin or RSL3 was determined as described in (B) and (C). See also Figure S1.

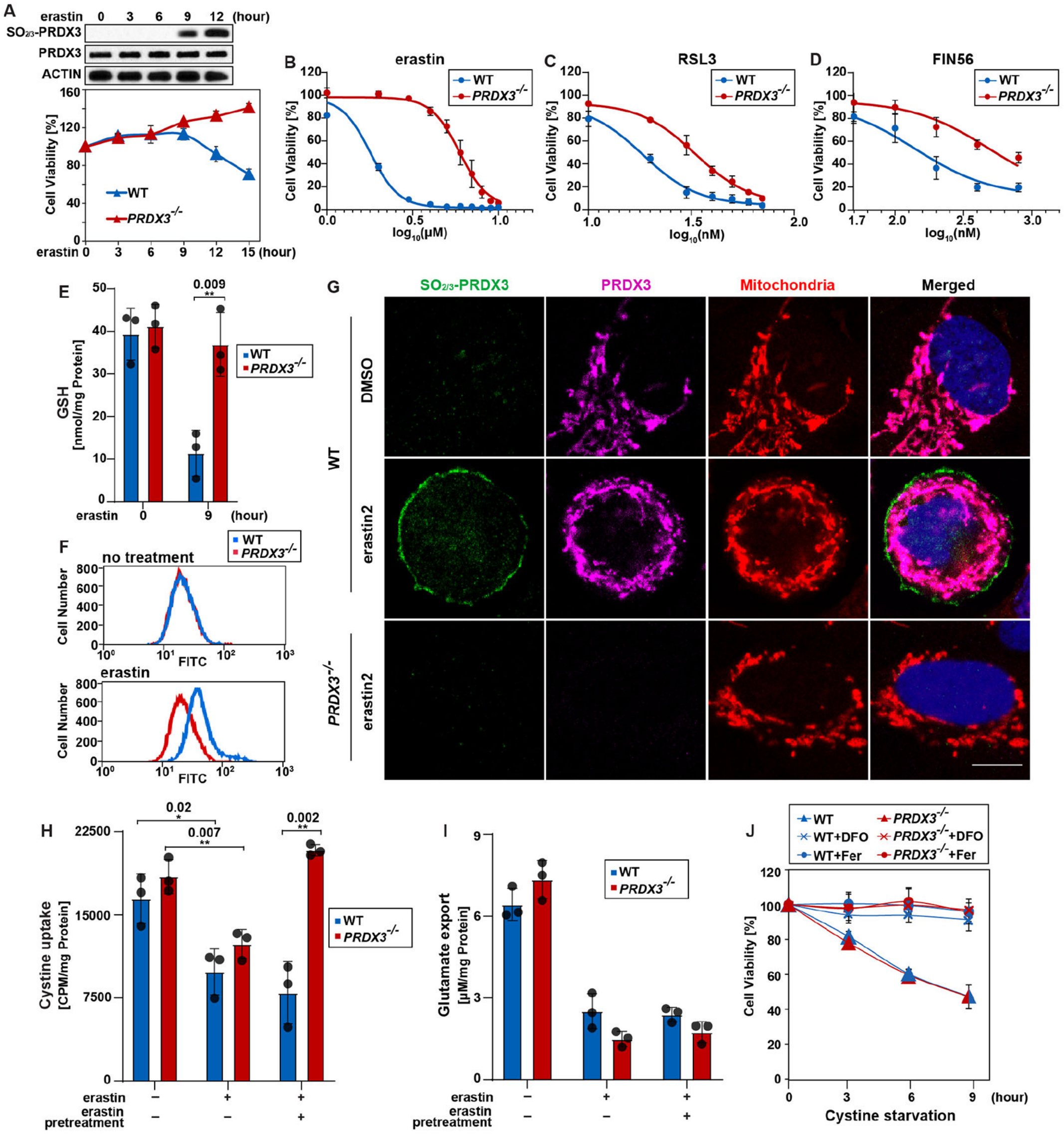

Figure 2. Hyperoxidized PRDX3 stimulates ferroptosis by inhibiting cystine uptake.

(A) The amount of hyperoxidized PRDX3 in indicated cells treated with 2 μM erastin for the indicated time was determined by immunoblot analysis (upper panel). Viability of indicated cells treated with 2 μM erastin for the indicated time was determined as described in Star Methods, with the value of the untreated WT cells set at 100% (lower panel).

(B-D) Viability of cells treated with indicated concentrations of erastin (B), RSL3 (C) or FIN56 (D) for 24 h was measured as shown in (A).

(E) The total amount of GSH in the indicated cells treated with or without 2 μM erastin for 9 h.

(F) BODIPY 581/591 C11 flow cytometry of the green fluorescence of indicated cells treated with or without 2 μM erastin for 12 h.

(G) Indicated cells treated with or without 200 nM erastin2 for 12 h were subject to immunofluorescent microscopy with indicated antibodies and MitoTracker. Scale bar=10 μm. Lower magnification of the images was present in Figure S2J.

(H and I) Cystine uptake (H) and glutamate export (I) of the indicated cells was measured as described in Star Methods in the absence or presence of 2 μM erastin pretreatment that prolonged the erastin treatment time to 9 h.

(J) Viability of the indicated cells starved for cystine in the absence or presence of deferoxamine (DFO, 50 μM) or ferrostatin-1 (Fer, 1 μM) for the indicated time was analyzed as described in (A).

(A-E and H-J) Results are reported as mean ± S.E.M. from three independent experiments. Statistical significance was calculated by unpaired, two-tailed t-test. See also Figure S2.

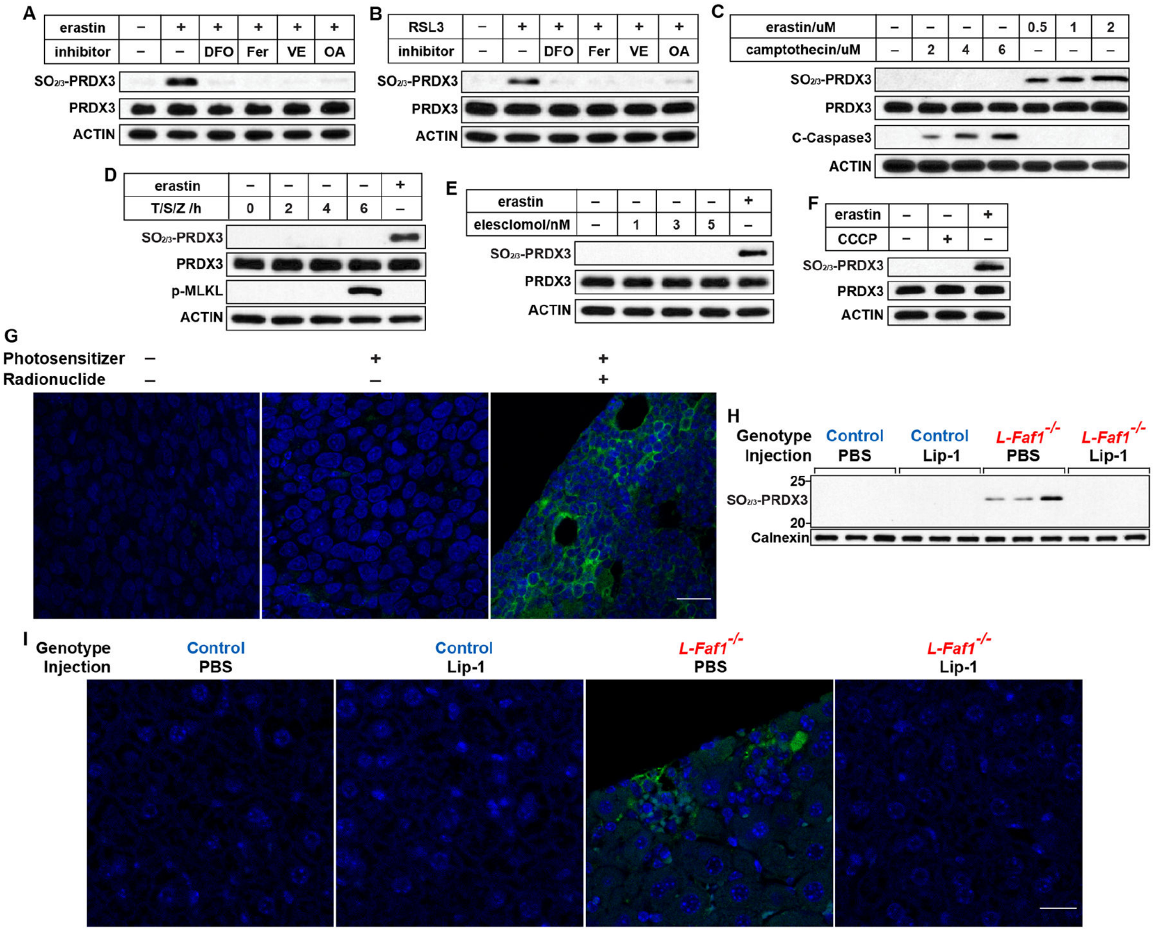

Figure 3. Hyperoxidized PRDX3 is specifically produced in ferroptotic cells.

(A and B) The amount of hyperoxidized PRDX3 in cells treated with 2 μM erastin (A) or 30 nM RSL3 (B) together with deferoxamine (DFO, 10 μM), ferrostatin-1 (Fer, 200 nM), vitamin E (VE, 10 μM), or oleate (OA, 200 μM) for 12 h was determined by immunoblot analysis.

(C) The amounts of hyperoxidized PRDX3 and cleaved caspase 3 (C-Caspase3) in SV589 cells treated with indicated concentration of erastin or camptothecin for 12 h were determined by immunoblot analysis.

(D) The amount of hyperoxidized PRDX3 and p-MLKL in HT29 cells treated with 20 ng/ml TNF-α, 100 nM SM164 and 20 μM z-VAD (T/S/Z) for the indicated time, or 2 μM erastin for 12 h was determined by immunoblot analysis.

(E) The amount of hyperoxidized PRDX3 in SV589 cells treated with 2 μM erastin or indicated concentration of elesclomol plus 2 μM $CuCl_2$ for 12 h were determined by immunoblot analysis.

(F) The amount of hyperoxidized PRDX3 in SV589 cells treated with 2 μM erastin or 4 μM CCCP for 12 h were determined by immunoblot analysis.

(G) Immunofluorescence of bone tissues containing xenograft multiple myeloma from mice subject to indicated therapy with the antibody that detects hyperoxidized PRDX3. Scale bar=20 μm. Lower magnification of the images was present in Figure S3D.

(H) The amount of hyperoxidized PRDX3 in livers from AA-fed control or *L-Faf1*$^{-/-}$ mice injected with Lip-1 or the control vehicle PBS.

(I) Immunofluorescence of livers from mice shown in (H) with the antibody that detects hyperoxidized PRDX3. Scale bar=20 μm. Lower magnification of the images was present in Figure S3E. See also Figure S3.

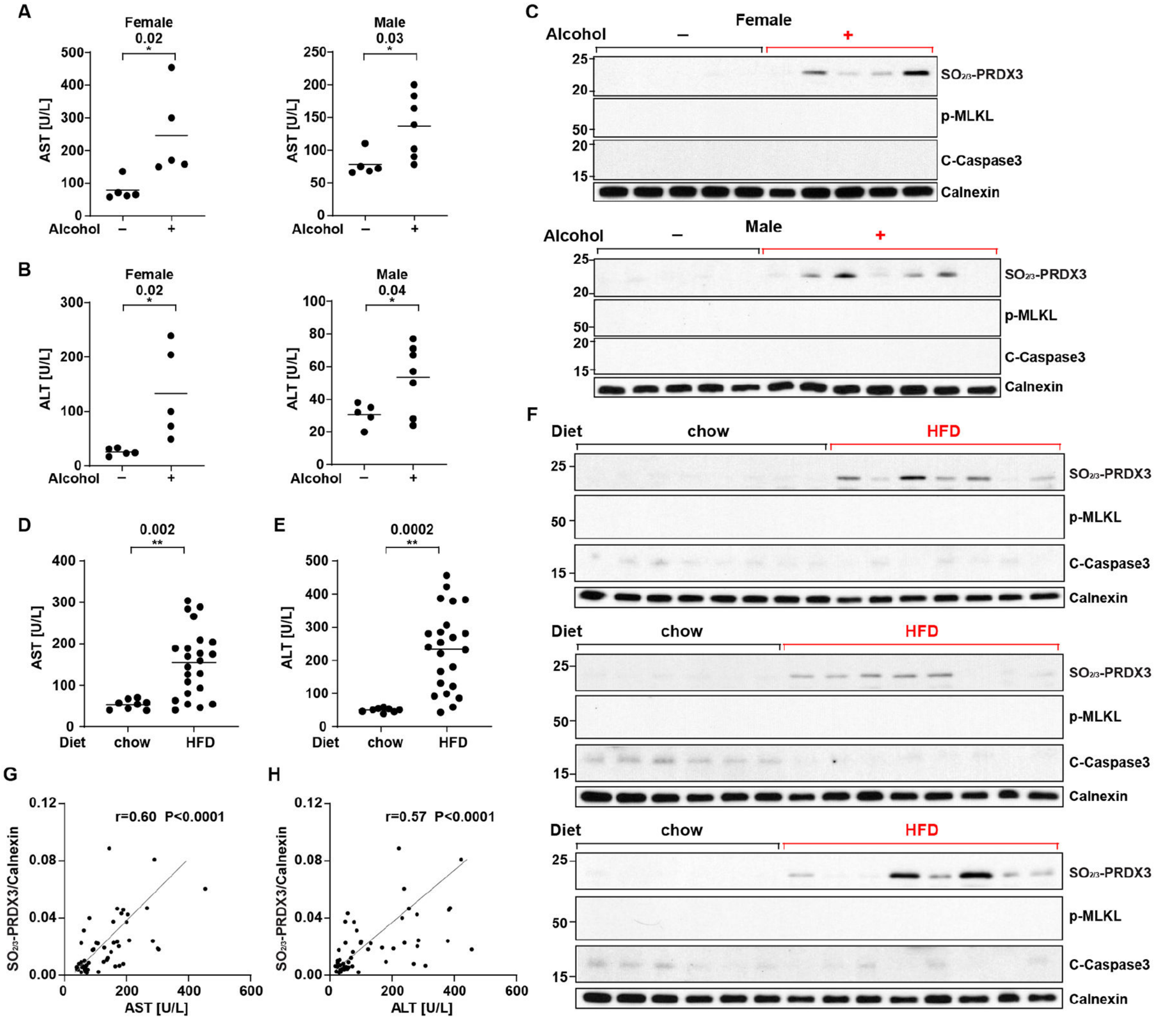

Figure 4. Hepatic damage in mouse models of AFLD and NAFLD is caused by ferroptosis.

(A and B) AST (A) and ALT (B) activities in serum of indicated female (n = 5) or male mice (n = 5-7) fed with alcohol or control liquid diets. Statistical significance was calculated by unpaired, two-tailed t-test.

(C) The amount of hyperoxidized PRDX3, p-MLKL, and C-caspase3 in livers from mice shown in (A) was determined by immunoblot analysis.

(D and E) AST (D) and ALT (E) activities in serum of mice fed with a chow (n = 8) or HFD diet (Research Diet D12451) (n = 23) for 12 weeks. Statistical significance was calculated by unpaired, two-tailed t-test.

(F) The amount of hyperoxidized PRDX3, p-MLKL, and C-caspase3 in livers from mice shown in (D) was determined by immunoblot analysis. For the HFD-fed group, each lane contained samples taken from different mice, and the results from all 23 mice were shown in three panels. For the chow-fed group, samples from all 8 mice were loaded on the first panel, from which those loaded in the first 6 lanes were reloaded in the second and third panels for comparison purposes.

(G and H) The correlation between AST (G) or ALT (H) values and that of the Li-COR-quantified hyperoxidized PRDX3 immunoblot signal (normalized against calnexin) in all the mice analyzed in A-F was determined by Pearson’s analysis.

Key resources table

REAGENT or RESOURCE	SOURCE	IDENTIFIER
Antibodies		
Rabbit anti-ACTIN	Sigma-Aldrich	Cat#A2066; RRID:AB_476693
Rabbit anti-Calnexin	Enzo Life Sciences	Cat#ADI-SPA-860-F; RRID:AB_11178981
Peroxidase AffiniPure Goat Anti-Mouse IgG (H+L)	Jackson ImmunoResearch	Cat# 115-035-003; RRID: AB_10015289
Peroxidase AffiniPure Goat Anti-Rabbit IgG (H+L)	Jackson ImmunoResearch	Cat#111-035-003; RRID:AB_2313567
Mouse anti-PRDX1	Thermo Fisher Scientific	Cat#LFMA0214; RRID:AB_1875494
Mouse anti-PRDX3	Thermo Fisher Scientific	Cat#MA5-33233; RRID:AB_2815371
Rabbit anti-PRDX1	Abcam	Cat#ab109498; RRID:AB_10865914
Rabbit anti-PRDX2	Abcam	Cat#ab109367; RRID:AB_10862524
Rabbit anti-PRDX3	Abcam	Cat#ab128953; RRID:AB_11143958
Rabbit anti-PRDX4	Abcam	Cat#ab184167; Clone:EPR15458(B)
Rabbit anti-PRDX5	Abcam	Cat#ab180587; RRID:AB_2904214
Rabbit anti-PRDX6	Abcam	Cat#ab133348; RRID:AB_11155931
Rabbit anti-$SO_{2/3}$-PRDX1-4	Abcam	Cat#ab16830; RRID:AB_443491
Rabbit anti-$SO_{2/3}$-PRDX6	Mybiosource	Cat#MBS6004332
Rabbit anti-SLC7A11	Abcam	Cat#ab175186; RRID:AB_2722749
Rabbit anti-mouse p-MLKL	Abcam	Cat#ab196436; RRID:AB_2687465
Rabbit anti-human p-MLKL	Abcam	Cat#ab187091; RRID:AB_2619685
Rabbit anti-cleaved caspase 3	Cell signal	Cat#9661; RRID:AB_2341188
IRDye® 800CW goat anti-rabbit IgG	LI-COR	Cat#926-32211; RRID:AB_621843
IRDye® 680LT goat anti-mouse IgG	LI-COR	Cat#926-68020; RRID:AB_10706161
Goat anti-mouse IgG (H+L) highly cross-adsorbed secondary antibody, alexa fluor plus 488	Thermo Fisher Scientific	Cat#A32723; RRID:AB_2633275
Rabbit anti-FAF1	Abcam	Cat#ab183045; Clone:EPR14754
Chemicals, peptides, and recombinant proteins		
FA-free BSA	Sigma-Aldrich	Cat#A7030; CAS:9048-46-8
(1S,3R)-RSL3	Cayman	Cat#19288; CAS:1219810-16-8
Nonidet P-40 alternative (NP-40)	Cayman	Cat#600009; CAS:9016-45-9
BODIPY 581/591 C11	Thermo Fisher Scientific	Cat#D3861; CAS:217075-36-0
Arachidonic acid	Nu-Chek Prep	Cat#U-71-A; CAS:506-32-1
Halt protease inhibitor cocktail (100X)	Thermo Fisher Scientific	Cat#87785
Erastin	Cayman	Cat#17754; CAS:571203-78-6
Erastin2	Cayman	Cat#27087; CAS: 1695533-44-8
FIN56	Cayman	Cat#25180; CAS:1083162-61-1
Deferoxamine	Cayman	Cat#14595; CAS: 138-14-7
Ferrostatin-1	Cayman	Cat#17729; CAS:347174-05-4
CCCP	Cayman	Cat#25458; CAS:555-60-2

REAGENT or RESOURCE	SOURCE	IDENTIFIER
SM-164	Cayman	Cat#28632; CAS:957135-43-2
TNF-α	Cayman	Cat#32020; UniProt Accession#P01375
Oleic Acid	Nu-Chek Prep	Cat#U-46-A; CAS: 112-80-1
Vitamin E (α-Tocopherol)	Sigma-Aldrich	Cat#258024; CAS:10191-41-0
Hoechst 33342	Thermo Fisher Scientific	Cat#H3570; CAS:23491-52-3
$CuCl_2$	Sigma-Aldrich	Cat#751944; CAS:7447-39-4
Elesclomol	Sigma-Aldrich	Cat#SML2651; CAS:488832-69-5
Z-VAD-FMK	Sigma-Aldrich	Cat#V116; CAS: 187389-52-2
^{14}C-Cystine	PerkinElmer	Cat#NEC854010UC
Ethanol	Fisher Scientific	Cat#04-355-453; CAS:64-17-5
Prolong glass antifade mountant with NucBlue stain	Thermo Fisher Scientific	Cat#P36985
MitoTracker Red CMXRos	Thermo Fisher Scientific	Cat#M7512
Fetal bovine serum, dialyzed	Thermo Fisher Scientific	Cat#A3382001
PRDX3(103-112) peptide	Genscript	Cat#SC1848
PRDX3(103-112) SO_3-modified peptide	Genscript	Cat#SC1848
Critical commercial assays		
Pierce BCA protein assay kit	Thermo Fisher Scientific	Cat#23225
Roche X-tremeGENE HP DNA transfection reagent	Sigma-Aldrich	Cat#6366546001
SuperSignal West Pico PLUS chemiluminescent substrate	Thermo Fisher Scientific	Cat#34580
CellTiter-Glo luminescent cell viability assay kit	Promega	Cat#G7570
GSH/GSSG-Glo assay kit	Promega	Cat#V6611
Glutamate-Glo assay kit	Promega	Cat#J7021
Experimental models: Cell lines		
Human: SV589 cells	Kept in Department of Molecular Genetics, UTSW	N/A
Human: A549 cells	ATCC	CCL-185
Human: HT1080 cells	ATCC	CCL-121
Human: Huh7 cells	Nakabayashi et al., 1982[36]	N/A
Human: HT29 cells	ATCC	HTB-38
Human: *PRDX3*$^{-/-}$ SV589 cells	This paper	N/A
Human: *PRDX3*$^{-/-}$*; pPRDX3* SV589 cells	This paper	N/A
Human: *FAF1*$^{-/-}$ SV589 cells	Shaojie et al., 2023[12]	N/A
Human: *PRDX5* overexpression SV589 cells	This paper	N/A
Human: *PRDX3*$^{-/-}$ HT1080 cells	This paper	N/A
Experimental models: Organisms/strains		
Mouse: C57BL/6J	Jackson laboratory	000664
Recombinant DNA		
pSpCas9(BB)-2A-Puro(PX459)-*PRDX3* sgRNA	This paper	N/A
pCMV-*PRDX3*	This paper	N/A

REAGENT or RESOURCE	**SOURCE**	**IDENTIFIER**
pCMV-*PRDX5*	This paper	N/A
pCDNA3.1-Hygro(+) (Empty vector)	Invitrogen	V87020
Software and algorithms		
GraphPad Prism 9	GraphPad Software	https://www.graphpad.com/
ImageJ	NIH, USA	https://imagej.nih.gov/ij/
FlowJo V10	BD Biosciences	https://www.flowjo.com/
LI-COR Image Studio	LI-COR	https://www.licor.com/bio/image-studio/
Other		
Control Shake and Pour	Bio-Serv	F1259SP
Ethanol Shake and Pour	Bio-Serv	F1258SP
Teklad global diet 2018	Envigo	2018
Research Diet D12451	Research Diets	D12451
Maltose dextrin	Bio-Serv	3585
35-mm glass bottom dish	Mattek	P35G-1.5-14-C